ADVANCED FUNCTIONAL MATERIALS
www.afm-journal.de

Infrared Spectral Emissivity Dynamics of Surfaces Under Water Condensation

Nicolas Lavielle, Ahmed M. Othman, Armande Hervé, Georges Hamaoui, Jipeng Fei, Jun Yan Tan, Frédéric Marty, Hong Li, Anne Mongruel, Daniel Beysens, Elyes Nefzaoui,* and Tarik Bourouina**

Water condensation on a surface strongly affects its effective emissivity, especially in the atmospheric window, a wavelength range essential for outdoor applications related to energetically passive cooling and heating. The evolution of emissivity of a silicon surface during dropwise and filmwise water deposition is studied. The evolution of the spectral radiative properties shows that the increase in effective emissivity due to the growth of a droplet pattern is steeper than for a growing water film of equivalent thickness. The change of surface emissivity takes place in the first moments of condensation where droplets as small as 10 µm drastically impact the reflectance of the pristine surface. The upper limit of effective emissivity is reached for a droplet radius or film thickness of 50 µm. During dropwise condensation, effective emissivity is weighted by the drop surface coverage and then remains within an asymptotic maximum value of 0.8, while in case of filmwise condensation, it is shown to reach 0.9 corresponding to water emissivity. Micrometer-scale spatially-resolved infrared spectral images enable to correlate the spatial variation of spectral properties to the droplet size and localization. Such findings are of interest to the implementation of moisture-controlled emissivity tuning and radiative sky-coolers for dew harvesting.

1. Introduction

In the context of reducing the carbon footprint of fossil fuels, interest is growing today for various applications involving energetically passive cooling and heating.[1] Spectrally selective emissivity/absorptivity of a material is a key surface property for radiative heat transfer engineering. The spectral requirements for emissivity are strongly dependent on its targeted use, where typical applications include solar thermal energy harvesting,[2–4] thermo-photovoltaics,[5,6] radiative cooling,[7,8] coherent thermal light sources[9] and dew water harvesters.[10–12] For instance, solar thermal energy harvesting requires maximum absorptivity in the spectral range ranging from ultraviolet to Short Wavelength Infrared (SWIR) (0.2–2.5 µm).[4] On the other hand, radiative cooling requires maximum emissivity in the so-called atmospheric window lying in the mid-wavelength infrared (MWIR)

N. Lavielle, A. M. Othman, A. Hervé, G. Hamaoui, F. Marty, E. Nefzaoui, T. Bourouina
ESYCOM lab
UMR 9007 CNRS
Univ Gustave Eiffel
Marne-la-Vallée 77454, France
E-mail: nicolas.lavielle@esiee.fr; elyes.nefzaoui@esiee.fr; tarik.bourouina@esiee.fr

A. M. Othman
Faculty of Engineering
Ain-Shams University
1 Elsarayat St. Abbassia, Cairo 11535, Egypt

The ORCID identification number(s) for the author(s) of this article can be found under https://doi.org/10.1002/adfm.202403316

DOI: 10.1002/adfm.202403316

J. Fei, J. Y. Tan, H. Li
School of Mechanical & Aerospace Engineering
Nanyang Technological University
Singapore 639798, Singapore

H. Li, T. Bourouina
CINTRA
IRL 3288 CNRS-NTU-THALES
Nanyang Technological University
Singapore 637553, Singapore

A. Mongruel, D. Beysens
Physique et Mécanique des Milieux Hétérogènes
CNRS
ESPCI
PSL Research University, Sorbonne Université, Université Paris Cité
Paris 75005, France

D. Beysens
OPUR, 2 rue Verderet
Paris 75016, France

(8–13 µm).[7] These requirements led to significant efforts in the past decade in designing dedicated meta-surfaces.[13–15] However, when used outdoor, the surfaces are subjected to varying weather conditions. In particular, surfaces can be exposed to water (e.g., dew condensers), whose intrinsic emissivity can strongly affect the radiative properties of the pristine surface. The deposition of water on an outdoor surface by condensation, rain or by other forms of moistening is indeed a daily-observed phenomenon. The deposition occurs on plants, soil, or artificial surfaces. Furthermore, the emissivity and wetting of surfaces can be strongly associated. This is for instance the case of dew water condensation induced by radiative cooling.[10–12] In this situation, a surface facing the sky passively experiences a temperature decrease through radiative cooling. Cooling is due to a negative radiative heat transfer with the outer space taking advantage of the atmosphere transparency, in particular between 8 and 13 µm. The larger the surface MWIR emissivity, the stronger the negative radiative heat transfer, and thus the energy-passive cooling effect.

Water is a scarce resource in arid and semi-arid climates. This problem is extending worldwide as a result of global warming and many efforts have been made to collect dew water as a source of fresh water. For this purpose, low-tech, energy-passive radiative coolers are often considered and most studies focus on the radiative properties of the surface under consideration.[16–18] The presence of condensed water on the considered surface in the form of droplets or films was however seen to significantly impact the radiative properties of the surface,[19,20] water and surface emissivities showing generally different values. This effect is somehow similar to the effects of water droplets in fog or in clouds on the IR sky emissivity.[21] Coming back to a wet surface as considered in this work, an effective emissivity[19] needs to be accounted for, as the surface is now partially (in case of dropwise condensation) or fully (in case of filmwise condensation) covered with water. During condensation, the effective emissivity of the surface evolves as a result of the combined emissivity of the pristine material surface and water.

Spectral measurements in the atmospheric window have already shown that the average emissivity of a plastic substrate increases when wet.[20] In the visible spectrum, the impact of dropwise condensation on the trajectory and polarization of light modified by an assembly of droplets, covering windows,[22,23] solar panels, or greenhouses[24] have been previously studied. A lack of knowledge remains regarding the spectrally-resolved effective emissivity of a wet surface in the MWIR spectral range. One has to mention, nevertheless, the pioneering works on the de-polarization of IR light by drops,[25,26] those on the analysis of the evolution of emissivity with condensation[27] and those revealing changes of radiative heat flux under condensation.[28] Furthermore, it has been shown, in the case of dropwise condensation, that surface coverage, droplets size, and droplets contact angles influence the effective emissivity of the substrate.[19,29]

Recent works addressed either the mean emissivity of a water droplet pattern, theoretically by Monte-Carlo tracing method[29] or experimentally and with a simplified model.[19] They, however, did not address the spectral emissivity nor filmwise condensation. The spectral emissivity of acrylic droplets was also recently investigated.[30]

These studies motivate the present detailed investigations of the reflectance and transmittance MWIR spectra in relation with dropwise condensation (Breath Figure pattern BF) and filmwise condensation, a situation not yet explored. In addition, spectral images of the droplets are obtained at a microscopic scale, which is a quite novel measurement. It allows pictures of the droplets to be observed with the contribution of the different parts of the drop to transmittance and reflectance. To this end, we study a sequence of water breath figures growing onto a flat surface. The corresponding droplet populations and effective radiative properties are investigated in the MWIR spectral range. Measured reflectance and transmittance spectra are analyzed with supporting numerical optical simulations of similar scenarios. We do not address their temperature dependence due to changes in the material optical properties, surface properties and electronic structure (the thermal variation of emissivity is 2.45×10^{-3} K^{-1} (Ref.[31]) and consider the radiative properties at 4 °C, a (constant) temperature value in our experiments, which is representative of dew condensation.

In contrast to the case of rain or fog deposition on a surface (which also impacts the surface radiative properties), it is important to note a subtle difference in the present experimental work. The formation of dew is indeed used to produce water droplets in a controlled manner. Note that in the present work, water condenses thanks to contact cooling. This cooling technique, which does not depend on the surface emissivity in contrast to radiative cooling, does not affect the characteristics of the condensed pattern (film or drops) and then the spectral emissivity of the surface. The case of a uniform water film is also studied, mostly theoretically, for comparison purposes. Numerical optical simulations and theoretical calculations give a comparison between the two extreme scenarios of dropwise and filmwise deposition and their influence on the dynamics of the absorptance spectra. Additionally, spectral radiative properties measurements with micron-scale spatial resolution are used to produce spatially-resolved spectral images of the BFs.

2. Results and Discussion

2.1. Evolution of the Spectral Radiative Properties with Dropwise Condensation

Figure 1 presents and characterizes 8 condensing BFs generated by condensing water vapor from humid air (90% RH) on flat silicon whose surface temperature is set at 4 °C. Condensation is interrupted by stopping the humid air flow at different times to obtain the successive BFs presented in Figure 1 and to perform spectral measurements. This experiment takes place under a FTIR (Fourier Transform Infrared) spectrometer equipped with optical microscope, which measures the spectral IR reflectance and transmittance. Figure 1 characterizes the BFs under study and correlates them with the measured IR spectral response and numerical simulations, presented in **Figure 2**. Figure 1a is a set of optical microscope images presenting the 8 BFs under study. Figure 1b gives the distribution of droplet radii r_i of each BF. Figure 1c presents, for each BF, the fraction of surface covered by the droplets (S/S_{tot}) and the evolutions of the Sauter mean radius $r_s = \frac{\Sigma r_i^3}{\Sigma r_i^2}$ for each BF pattern. The same condensation experiment under IR spectrometer – microscope has been performed on modified silicon wafers with PTFE (Teflon) and SiO_2 surfaces

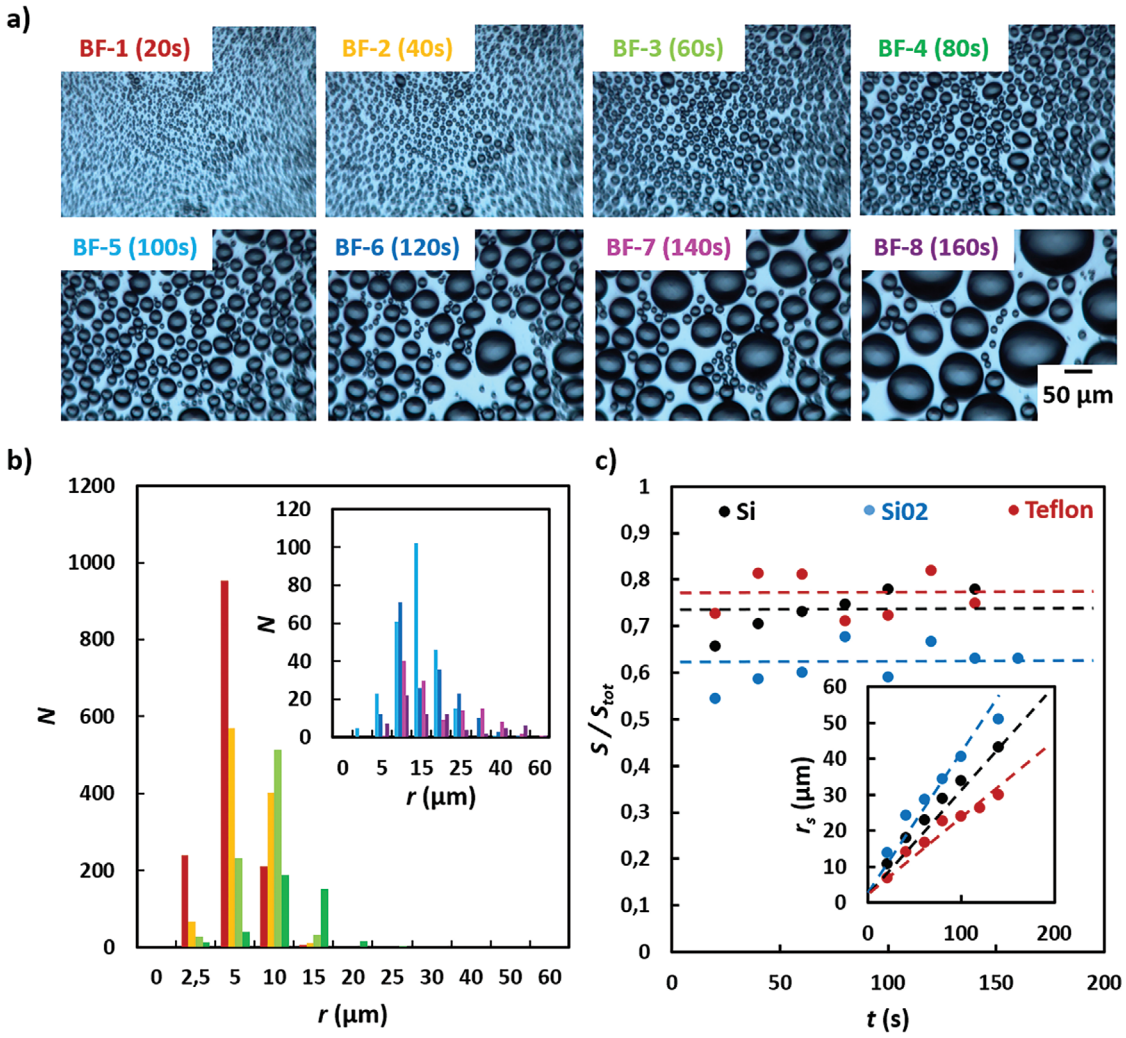

Figure 1. Breath figures evolution and characterization: a) Optical microscope images of the 8 breath figures (BFs) on silicon wafer (Si). b) Droplet size distribution of BFs of the patterns shown in (a) (number of droplets, N, of radius, r, in 5 µm steps). The same colors codes as in (a) are used in (b) for BF1 to BF4 and in its inset for BF5 to BF8. c) Droplet Surface coverage (S/S_{tot}) and inset: Sauter mean radius (r_s) of the BFs on silicon wafer (Si), SiO_2, and PTFE (Teflon) surface coatings.

to evaluate the impact of the wetting properties. Figure S1a (Supporting Information) indicates the thicknesses of Teflon and SiO_2 and the water contact angles (CA): CA = 70°, 91°, and 48° for Si, Teflon and SiO_2, respectively. For Si, in Figure 1b, the size of the droplets increases with condensation time, we can also observe a bimodal distribution from BFs 6 to 8, which is the sign of re-nucleation events in the free space left by the coalescences of neighboring droplets. In Figure 1c, for the three surfaces, a plateau for the surface coverage is rapidly reached after 50 s of condensation, with a value of ≈ 0.75 for the Si surface and r_s evolution is found to scale linearly with time, in agreement with theory.[11] In Figure 1c, the plateau value of S/S_{tot} (dashed) increases with an increase of the CA, whereas r_s decreases with an increase of the CA. The droplet size distribution and the values of S/S_{tot} and r_s characterize each BF under study and will be used as the determining parameters for numerical simulations and for the global understanding of the IR spectral response. Focusing on the impact of surface chemistry, one notes in Figure 1c that the plateau of S/S_{tot} (dashed) increases with an increase of the CA, whereas r_s always decreases with an increase of the CA. This result can be explained in terms of a second nucleation of BF pattern in the space left free between the large drops. A higher drop contact angle generates smaller droplet radius for a constant volume of condensed water, more space free between drops, and leads to smaller surface coverage in the auto-similar regime as it is well-known.[11] However, upon re-nucleation, the new nucleated droplets in the free space between drops lead to an actual increase of the total surface coverage.

Figure 2 presents the evolution of the IR spectral response of BFs on Si from Figure 1. For Teflon and SiO_2, the reflectance, transmittance, and the corresponding BFs optical images can be found in Figures S2 and S3 (Supporting Information), respectively. Figure 2 is organized as follows: In the first row, Figure 2a reports the measured relative spectral reflectance R/R_0 as a function of the wavelength in the 2.5 – 14 µm range for the 8 breath figures of Figure 1 on Si, where R_0 is the reflectance of the bare

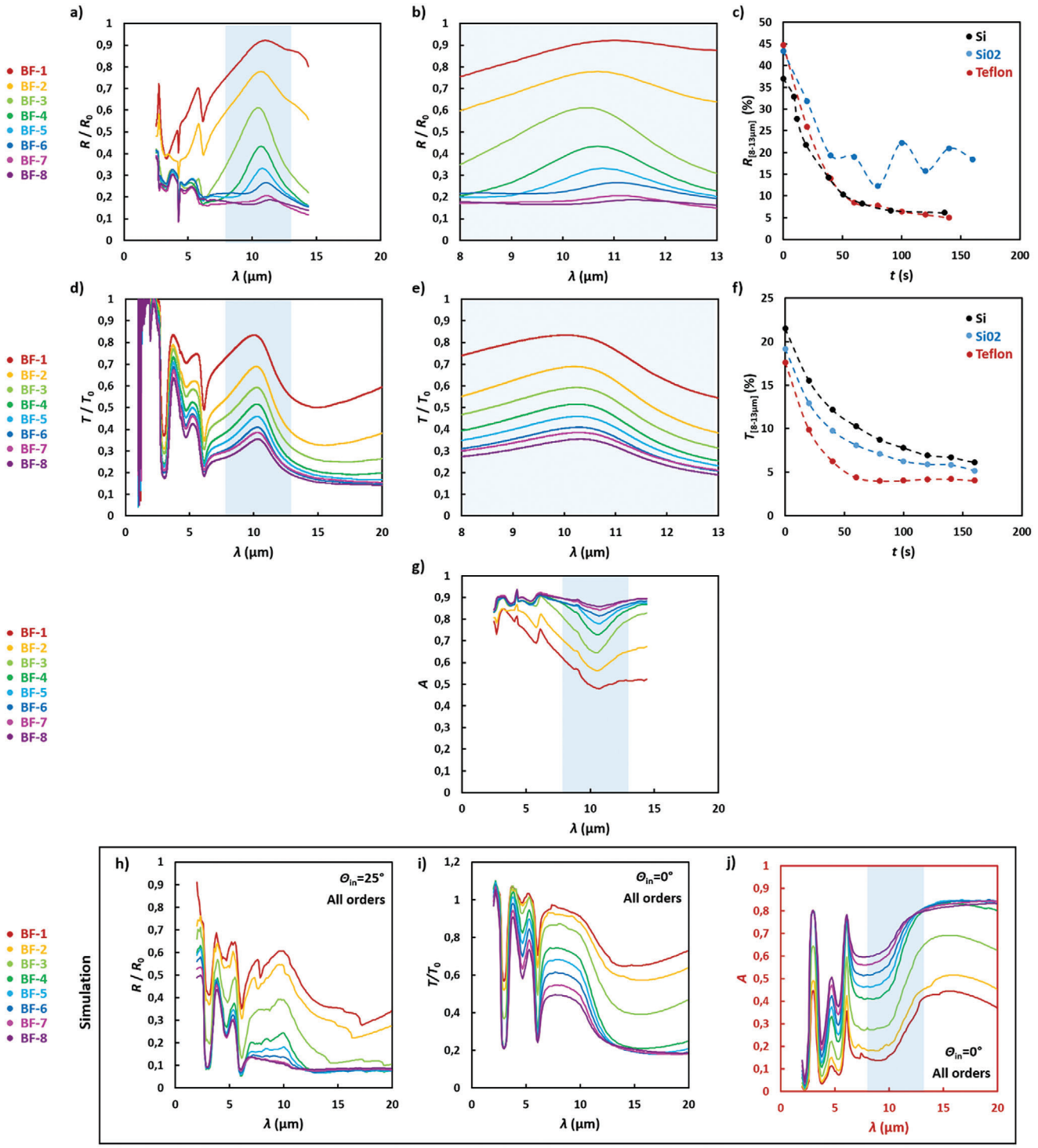

Figure 2. Spectral IR response during the breath figures evolution (same 8 BFs of Figure 1): a) Relative reflectance R/R_0 as a function of IR wavelength (R_0 is the bare Si reflectance). b) Zoom in the atmospheric window. c) Average reflectance in the atmospheric window ($R_{[8-13\ \mu m]}$) as a function of condensation time for Si, SiO_2 and Teflon surfaces. d) Relative transmittance T/T_0 as a function of IR wavelength (T_0 is the bare Si transmittance). e) Zoom in the atmospheric window. f) Average transmittance between 8 and 13 μm ($T_{[8-13\ \mu m]}$) as a function of condensation time for Si, SiO_2 and Teflon surfaces. g) Absorptance A as a function of IR wavelength. h–j) Results from rigorous coupled-wave analysis (RCWA) numerical simulation of the spectral evolution of Si substrates with water droplet distributions as in Figure 1. (b): relative reflectance, R/R_0 (h), relative transmittance, T/T_0 (i) and absorptance, A (j).

Si (before condensation) Figure 2b is a focus of Figure 2a in the atmospheric window (8-13 µm). Figure 2c gives the average value of absolute reflectance R between 8 and 13 µm for Si, SiO_2, and Teflon as a function of condensation time (cumulative time during which condensation proceeds). The second row of Figure 2 is organized the same way as the first row, giving the results of relative surface averaged spectral transmittance, T/T_0. T_0 is the reflectance of the bare Si. The third row of Figure 2 shows the results from numerical simulations of the relative reflectance R/R_0, relative transmittance T/T_0 and absorptance A, for Si. Figure S1b,c (Supporting Information) presents the raw values of measured reflectance and transmittance, respectively, for the three bare surfaces before starting condensation.

Regarding reflectance evolution, one observes a global decrease in the whole wavelength range with condensation time, with a saturation starting at BF 7 (140 s). When focusing on the atmospheric window, one can observe a large reflectance peak. The peak decreases and slightly shifts to longer wavelengths with condensation time. The same general observations can be made for the transmittance spectra. The reflectance and transmittance evolution behavior are the same with Teflon (Figure S2, Supporting Information) and SiO_2 (Figure S3, Supporting Information). The main evolving peak is located in the atmospheric window. One can correlate the slightly varying position of this peak to the size of the water droplets, whose distribution evolves with time and whose order of magnitude lies in the same range as the wavelength of the IR irradiation. The slight shift to higher wavelengths can be attributed to the increase of the droplets size, suggesting a light scattering effect. Regarding the evolution of the average value of reflectance in the atmospheric window (Figure 2c), a sharp decrease of its value is observed in the first seconds of condensation for the three surfaces (with a similar initial decreasing slope). After 50 s of condensation, the reflectance saturates toward its minimal value. This result indicates that the change of surface emissivity takes place in the first moments of condensation where droplets as small as 10 µm are sufficient to drastically impact the reflectance of a surface.

Concerning the impact of surface coating, the average value for reflectance on SiO_2 is significantly higher at equilibrium (20% vs 5% for Si and Teflon). This result is due to the lower value of surface coverage ($S/S_{tot} = 0.6$) for SiO_2 as compared with values above 0.75 for Si and Teflon. Indeed, a lower surface coverage exposes a higher pristine surface for reflection. The fluctuations of the reflectance observed with the SiO_2 surface could be attributed to the fluctuations of surface coverage with condensation time as seen in Figure 1c. Comparing Si and Teflon, the average reflectance value at equilibrium is similar for both surfaces. However, the initial value of reflectance for Si is slightly lower than the Teflon reflectance. The same value at equilibrium for both surfaces is attributed to the slightly higher surface coverage on Teflon.

Regarding the evolution of $T_{[8-13\mu m]}$ for the three surfaces (Figure 2f), all transmittance values decrease with condensation time with similar behavior and look close to an equilibrium value after 100 s of condensation. More condensation time is thus needed to ensure that transmittance does not continue to slowly decrease. As surface coverage reaches a plateau after 50 s of condensation, one attributes the further decrease of transmittance to the increasing size of the droplets. One notes that droplets whose size is as small as 30 µm strongly lower transmittance. Interestingly, the reflectance saturates faster than the transmittance, which indicates a stronger dependency for transmittance on droplet size. Lastly, the different values of transmittance for the three surfaces can be explained by the initial value of transmittance before condensation. Additionally, Figure 2g presents the spectral absorptance $A = 1 - T - R$ for the eight BFs; it displays saturation for times later than BF6.

To further investigate the role of surface coverage and droplets size on the reflectance spectra, Figure S4 (Supporting Information) presents another condensation experiment performed on Si with varying surface coverage (Figure S4a, Supporting Information) and Sauter mean radius r_S (Figure S4b, Supporting Information). The particularity of this experiment is that the surface coverage evolves slowly to its equilibrium value, which allows us to differentiate more easily the impact of surface coverage and droplet size. Figure S4c,d (Supporting Information) presents the evolution of the value of the reflectance at a wavelength of 10 µm as a function of S/S_{tot} and r_S, respectively. One observes that for a constant value of S/S_{tot} ($t > 50$ s) the reflectance still decreases, which indicates that the reflectance is still impacted by the size of the droplet. Nevertheless, Figure S4a,d (Supporting Information) shows that once the surface coverage has reached its equilibrium value, after point BF4 (45s) –also corresponding to droplet radius r_s above 10 µm, the variation of the reflectance with r_s slows down to eventually saturate when r_s reaches 20 – 30 µm at times 50–60 s. This complementary result confirms the previous findings of Figure 2c.

We have also performed numerical simulations considering the radius distribution and surface coverage of the BFs in Figure 1. The basis and the details of the simulation of transmittance and reflectance of droplets on Si are reported below in the Experimental Section. The simulation uses the S4[32] implementation of the rigorous coupled-wave analysis (RCWA). We present in Figure 2, row 3, the simulation results concerning the evolution with the 8 BFs of the relative spectral reflectance (Figure 2h), the relative spectral transmittance (Figure 2i), and the spectral absorptance (Figure 2j). The absorptance was derived from the conservation of energy, $A = 1\text{-}R\text{-}T$, and the Kirchhoff's law for thermal radiation was used, giving spectral emissivity equal to spectral absorptivity. The results from the simulation capture well the tendency of decrease of the reflection and transmission with condensation time. The presence of the peak in the atmospheric window is also captured by the simulation for the relative reflectance and transmittance. The slight shift of this peak can be found in the reflectance simulated spectra, whereas it is not the case for the transmittance. In this regard, Figure S5 (Supporting Information) shows simulation of transmittance using "Cone 5" (±5° angular span) instead of "all orders" (all angles captured by the detector), fairly captures the shift of the peak in the atmospheric window. The values of the relative reflectance and transmittance from the simulation agree with the experimental ones. We show in Figure 2j that the absorptance increases with condensation time and saturates after 100 s of condensation, which compares well with the experimental data. However, the values of the simulated absorptance are lower than the experimental values, because in the simulation only a single air/Si interface is considered, and thus the global contribution of the silicon wafer to the reflectance (multiple interface reflection) and

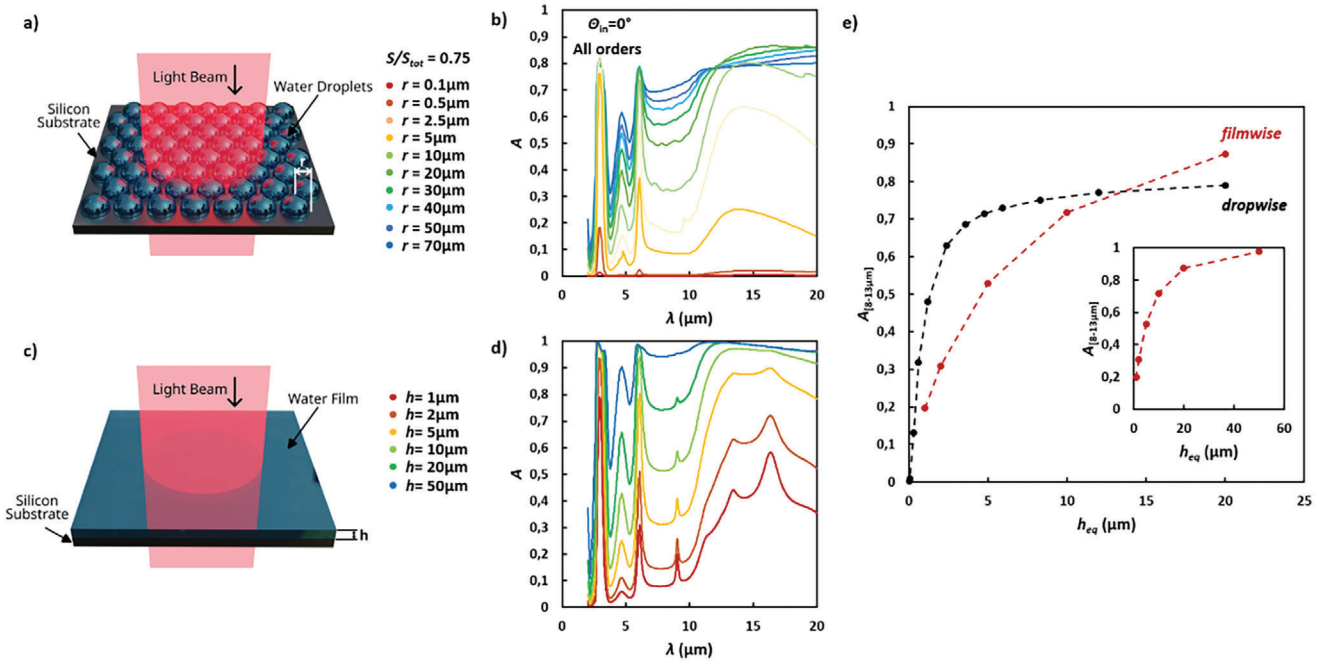

Figure 3. Dropwise versus filmwise water deposition. a,c) Schematic illustrations on silicon substrate of (a) an array of water droplets of varying radius, r, at surface coverage $S/S_{tot} = 0.75$ and (c) a film of water of varying thickness, h. b) Evolution of absorptance (A) spectra modeled by RCWA numerical simulation for an array of droplets of varying r. d) Evolution of A for a film of water of varying h. e) Evolution of the average absorptance in the atmospheric window ($A_{[8-13\ \mu m]}$) for dropwise and filmwise water deposition as a function of the same total volume of water per unit surface area, that is, the equivalent film thickness, h_{eq}. The inset of (e) is the filmwise absorptance evolution shown for an extended range of h_{eq}.

transmittance (transmittance through the silicon wafer thickness) is not accounted for. The absorptance of the silicon is therefore under-estimated by the RCWA simulation.

2.2. Spectral Emissivity: Dropwise Versus Filmwise Deposition

Figure 3 presents the simulated (droplets) and calculated (film) absorptance evolution as a function of droplet radius or film thickness, respectively. For droplets, the rigorous coupled-wave analysis (RCWA) numerical simulation was used to simulate the influence of droplet size, for a constant surface coverage, on the absorptance spectra. For this simulation, an array of hemispherical droplets of the same radius, r, varying from 0.1 to 70 µm with a surface coverage S/S_{tot} fixed at 0.75 (case of condensation on Si) was considered to evaluate the only contribution of droplet size on the absorptance spectra. Figure 3a gives a schematic representation of the pattern of droplets and Figure 3b presents the simulated absorptance spectra of droplets as a function of droplet radius, r, with an incidence angle of 0° and considering all diffraction orders. The absorptance, A, was derived from the values of the simulated reflectance and transmittance. Absorptance generally increases with increasing droplet radius. Droplet size r = 0.1 or 0.5 µm slightly affect the spectral response, whereas the absorptance is drastically increasing for larger droplets size, saturating for $r \approx 50$ µm. This simulation confirms the experimental results presented in Figure 2, which outlines that the change in emissivity takes place in the first moments of condensation, to finally saturate for droplet size ≈50 µm. Note that the change in emissivity takes particularly place in the atmospheric window and thus will largely impact the radiative heat transfer of surfaces covered by water droplets. For comparison, filmwise water deposition was also considered. Figure 3c is a schematic representation of the studied system composed of a water film of varying thickness, h, between 1 µm and 50 µm. For the case of the water film, the calculations of reflectance and transmittance were carried out as follows. The water film calculations assumed a normally-incident incoherent radiation on the structure, where the reflectance and the transmittance of the multi-layer structure was calculated using the incoherent case of the transfer matrix method,[33] using the refractive index and extinction coefficient (imaginary part of the refractive index) of silicon[34] and water[35] as a function of wavelength. For simulation/experiment comparison purposes, a set of three experiments was carried out with water film thicknesses of 6, 20, and 40 µm trapped between silicon slabs separated by microbeads spacers defining the water film thickness. The experimental details are given in the Experimental Section. For these three systems, transmittance was measured with a spectrometer, and Figure S6a (Supporting Information) gives a schematic representation of the studied system along with the results for measured and calculated transmittance. Figure S6a (Supporting Information) shows that the calculated spectra agree well with the measured spectra, validating the calculation method. This method was then applied to the configuration of Si/water/air. Figure S6c,d (Supporting Information) presents the calculated transmittance and reflectance spectra, respectively, for the water films considered in Figure 3c. Figure 3d gives the corresponding calculated absorptance spectra (derived from the calculated reflectance and transmittance shown in Figures S6c,d, Supporting Information) for a water film of various h. A film

thickness of 1 µm is shown to significantly impact the absorptance spectra, and an increase of h leads to a significant increase in absorptance until a maximum value near unity is reached for $h \approx 50$ µm. Both Figures 3b,d show that the spectral response is largely influenced by the presence of water droplets or water films in the entire spectral range and in particular in the atmospheric window. For the film case, a near unity emissivity is reached as the surface is fully covered with water ($S/S_{tot} = 1$), whereas in the case of droplets an earlier saturation takes place due to the saturation of the partial surface coverage by the drops. In the case of drops of constant surface coverage, simulation results confirm that the size of the droplets impacts the absorptance spectra, which nevertheless saturates at ≈50 µm drop radius. In the case of a water film, saturation is reached also for a film thickness of 50 µm, for which the emissivity of water is reached. Figure 3e gives the average absorptance in the atmospheric window between 8 and 13 µm ($A_{(8-13\ \mu m)}$) as a function of the total volume of water per unit surface area (the equivalent thickness, h_{eq}), for a fair comparison between the dropwise and filmwise deposition of water. One can observe that the absorptance in the atmospheric window increases faster in the case of droplets, compared to the film, for $h_{eq} \approx 5$ µm. Indeed, for an equal volume of deposit water, droplets radii are larger than the equivalent film thickness and thus impact more drastically the absorptance. Since the droplet surface coverage does not reach unity, in contrast to the film, above some thickness ≈13 µm the film becomes more absorbing. This finding shows that the geometry of the drops strongly influence the reflectance and transmittance spectra, as discussed in Figure 2. The inset of Figure 3e indeed shows that saturation to pure water absorptance is reached only for a film thickness of 50 µm. Finally, it is important to note that for dropwise deposition, the value of saturation of the absorptance is ≈0.75, which is close to the value of the assumed surface coverage of 0.75. This result indicates that, upon saturation, water droplets act similarly to a film of water.

Another noticeable difference between dropwise and filmwise condensation is the spectral shape of the emissivity and its evolution. In case of filmwise condensation, the spectral emissivity depends solely on molecular water absorption. Accordingly, the shape of the spectral emissivity does not change while increasing the water height; only its magnitude increases as shown in Figure S6 (Supporting Information). However, in case of dropwise condensation, an additional mechanism beyond the molecular scale is involved. Indeed, light scattering effect is non-negligible as the size of the droplets fall in the same range of the wavelength of the infrared light.[36] Consequently, not only the magnitude varies, but also the shapes of the spectral reflectance, transmittance, and emissivity are deformed (Figure 2b,e,g) during the evolution of droplet size distribution (Figure 1b; Figure S4b, Supporting Information). We confirmed these observations through other experiments conducted on Teflon-coated silicon surfaces (Figure S2, Supporting Information) and SiO2-coated surfaces (Figure S3, Supporting Information). The evolution of droplet size distribution involves coalescence of neighboring droplets. The coalescence dynamics on a pristine silicon surface can be assessed from Figure S4b (Supporting Information), where one can see that the Sauter radius r_s increases from 5 to 42 µm within 130 s. An indicator on the impact of this variation on the emissivity can be seen in Figure S4d (Supporting Information), showing a drastic decrease of reflectance from 33% to 5% during the same sequence. Furthermore, as shown in the black curve of Figure 3e, the corresponding trend for emissivity is an increase with the equivalent water height h_{eq} and then stabilization below 80%.

Figure S7 (Supporting Information) presents the simulation results for the absorbance of an array of droplets of $r = 10$ µm (with $S/S_{tot} = 0.75$) at different angles of incidence (0, 20, 40, 60, and 80°) to address the directional effects on the emissivity/absorptivity of a droplet-covered surface. For relatively small angles of incidence (<20°), it can be observed that the angle of incidence has a small effect on the simulated absorbance of the system, and the emissivity slightly increases, which agrees with literature.[30] For large angles, however, the scattering effects of the droplets increase and exhibit a wavelength dependence, as the droplets act as a diffraction grating diffracting light, where more diffraction orders can be excited in the case of a larger angle of incidence.

Figure S8 (Supporting Information) presents the evolution of calculated radiative cooling power associated to the evolution of the absorptance during both dropwise (Figure S8a, Supporting Information, from the spectra of Figure 2g) and filmwise (Figure S8b, Supporting Information, from the spectra of Figure 3d) water deposition. Calculations were performed according to the equations developed in Ref.[13] considering a surface and an ambient temperature of 30 °C. Conduction, convection, and solar irradiance were neglected (details in Note S1, Supporting Information). Standard atmospheric IR transmission spectra were used. The situation is, however, more complex in the reality since the atmosphere emissivity exhibits an angular dependence, minimum at the zenith (≈0.62) and maximum near the horizon (≈1). One also has to account for always existing near-horizon IR emitting obstacles and the fact that the surface under study can present a tilt angle with horizontal. A detailed analysis of a surface radiative deficit taking into account these parameters can be found in reference.[37]

Figure S8a,b (Supporting Information) shows that the presence of water on a silicon surface greatly influence the radiative cooling ability. The cooling power increases with the evolution of the BFs or with increasing water film thickness and saturation is reached for a typical drop/film size of 50 µm, such as the emissivity does. The order of magnitude of the calculated radiative cooling power is ≈ 100 W m^{-2}, which is consistent with the order expected for a black body emitter. It is worth mentioning that the scenario under consideration starts with a pristine silicon surface of rather small emissivity. As a consequence, in this case, water condensation leads to the improvement of cooling power along with an increase of emissivity. In another theoretical extreme case of a perfect black body surface (emissivity ~ 1), the impact of condensation of water (of emissivity ~ 0.95) would be less severe. Indeed, in such case, the effective emissivity of the black body surface would decrease during water condensation process, tending toward the emissivity of water weighted by the water surface coverage, with an effective emissivity remaining in the range of 0.95–1. In this scenario, dropwise condensation would have less impact than filmwise condensation since the latter eventually tends toward the asymptotic value of water emissivity. In both cases, as a result of the water-induced slight decrease of emissivity, the cooling power would also slightly decrease. However, one remains in a high emissivity range and therefore water

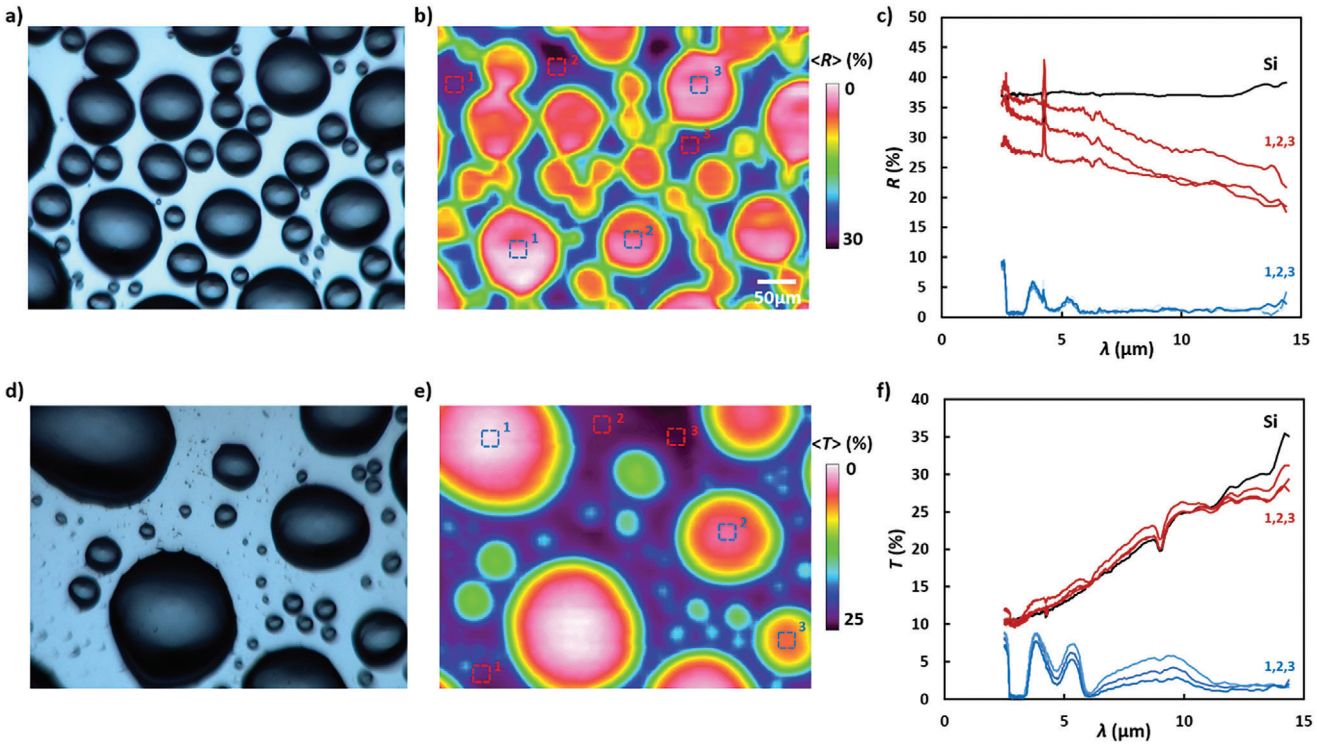

Figure 4. Droplets local contribution to spectral emissivity: Optical microscope images of the breath figures patterns a) and d) and corresponding reflective b) and transmissive e) spectral images. The color code uses average values of reflectance (<*R*>) or transmittance (<*T*>) from 2.5 to 14 μm wavelengths with a resolution of 6.25 × 6.25 μm (scale bar of 50 μm applies to the four images). c) Reflectance, *R*, and f) transmittance, *T*, spectra of the three red dotted square regions located in between droplets, of the three blue dotted square regions located on the center of droplets and of bare silicon (Si) (before condensation, in black color).

condensation should have a minor impact on emissivity/cooling power of a black body surface.

2.3. Spatially-Resolved Droplets Contribution to Emissivity

Figure 4 investigates at high spatial resolution the contribution of water droplets on the reflectance and transmittance spectra. In this regard, two BFs were studied, one for reflectance and the other for transmittance, setting the imaging pixel size to its minimal value 6.25 μm. As noted in section "Experimental Section – Spectral reflectance and transmittance measurements using FTIR microscopy imaging", it was not possible to use in the transmittance measurements the very same breath figure pattern as with the reflectance measurements because the setup could not keep the surface temperature low enough to prevent evaporation. The droplet evaporation is, however, slow enough such as it affects only marginally the BF pattern, as shown in Figure 4 where tiny droplets are still present. The dimensions of the optical images presented in Figure 4 are 350 × 450 μm, which means that the spectroscopic measurement will give 4032 reflectance or transmittance spectra per image. The assessment of the 4032 spectra allows us to reconstruct a spatially-resolved spectral image of the BFs, with a resolution of 6.25 μm. Figure 4b shows the reflectance spectral image of the optical image of Figure 4a,e, is the transmittance spectral image of the optical image of Figure 4d. The BFs have been generated by condensation on a 1 × 1 cm^2 silicon wafer.

One notes that the spectral images well correspond to the optical image. The spectral images enable a spatial resolution of the IR spectral radiative properties. In both Figure 4b,e, we have selected 3 areas with dimensions of 6.25 × 6.25 μm located on a bare part of the silicon wafer (red dotted squares) and 3 other areas located at the center of 3 droplets (blue dotted squares). For each defined area, the associated reflectance and transmittance spectra are plotted in Figure 4c,f, respectively. For comparison, the reflectance and transmittance spectra on bare silicon (before condensation) is as well plotted in black color. In Figure 4c, when located on droplets, one can observe that the reflectance spectra of the three blue curves (which superimpose) are far below the spectra of bare Si and close to the water reflectance. When located in between droplets on bare silicon, the spectra are close to the bare Si spectra. There is nevertheless a difference between the curves between the drops and the bare substrate, increasing with the wavelength. It indicates that the reflectance is impacted by the nearby droplets. The spatial resolution of 6.25 μm of the FTIR microscope is defined for a wavelength range of IR light below the wavelength $\lambda = 6.25$ μm. Above this value, the limit of diffraction applies, and the size of the scanned area is equal to the wavelength of the IR light (Rayleigh criteria). Thus, the resolution gets worse with increasing wavelengths ($\lambda > 6.25$ μm), leading to a larger collection spot for the longer wavelengths. In this case, as the collection spot increases for larger wavelengths, collection of the average spectra is more sensitive to surrounding droplets as the wavelengths increases; which leads to the decrease of the

reflectance with increasing wavelengths. Regarding the discrepancies between the red plots of Figure 4c, they are due to the relative proximity of water droplets to the scanned area. Indeed, the closer the water droplets are to the scanned area, the stronger the decrease of reflectance will be.

For transmittance, when located in between droplets, the red spectra almost superimpose with the one of bare Si, in contrast to reflectance. An explanation would be that the relative proximity of water droplets to the scanned area for transmittance is weaker than the one for reflectance, leading to average spectra non-impacted by surrounding droplets. When located on droplets, the blue spectra of transmittance decreases as it would do for pure water. The transmittance and the reflectance are thus both impacted locally by the presence of the droplets. It indicates that the water droplets largely impact reflectance and transmittance at global and local levels. Such spectral images, along with the measured, simulated and calculated data of reflectance and transmittance; underline the local and global contributions of the presence of water to the spectral radiative properties dynamics in general, and spectral emissivity in particular, when droplets evolve on any surface.

3. Conclusion

As the emissivity of water in the atmospheric window (8—13 µm) is near unity, water deposition on any surface will substantially impact its emissivity. Water can be deposited in the form of droplets or film by, for example, rain, fog, or vapor condensation. Surfaces can reach temperatures below the dew point temperature by radiative cooling, which triggers dropwise or filmwise condensation. This work reveals the evolution of IR spectral properties during water condensation. The presence of evolving droplet patterns or growing water film is shown to impact the spectral radiative properties of the surface and in particular its effective emissivity. Droplets, with radius as small as 0.5 µm, decrease the reflectance and transmittance in the atmospheric window, which results in an increase of the absorptance. This increase is steeper at the first moments of condensation and saturates when droplets radius is in the order of 50 µm. It is interesting to observe that both the reflectance and transmittance spectra display a peak in the atmospheric window, which decreases with increasing droplet radius and slightly shifts to the longer wavelengths when the droplet size is comparable to the incident light wavelength. The value of the absorptance at saturation mostly depends on the drop surface coverage and on the absorptance value of the bare material. Wetting properties of the surface influences the emissivity of the surface, as higher droplet contact angles lead to a higher plateau surface coverage at saturation, which is the main governing parameter at saturation. Furthermore, we showed that Sauter mean radius was correlated to the reflectance values. Indeed, Sauter radius includes droplet size and surface coverage. Its calculation could thus enable the determination of a given BF reflectance.

In the case of a growing water film, the increase of the absorptance in the atmospheric window is slower than for the case of droplets for an equivalent volume of water per surface area. The film absorptance is shown to saturate for a thickness of 50 µm, where it reaches the value of pure water. For droplets, saturation is reached for drop radii ≈50 µm, corresponding to an equivalent film thickness h_{eq} ≈5 µm, with absorptance value depending on the drop surface coverage. One notes that, for dropwise deposition, the value of saturation of the absorptance is close to the value of the surface coverage indicating that, upon saturation, water droplets act similarly to a film of water.

The measurements of the spectra by IR spectrometer have been supported by numerical simulations and calculations, which permits to separate the contribution of water droplets or water films from the surface emissivity. Furthermore, spectral images of reflectance and transmittance with a resolution of 6.25 µm give the spatial variation of spectral properties and allow a correlation to be made with droplet size and location. Such spatially-resolved spectral images could be used to determine the thickness profile of droplets based on the IR spectral response.

As the emissivity of the surface rapidly reaches the water emissivity value (weighted by the surface coverage), the bare surface emissivity is not the determining parameter in the steady-state operation. As a matter of fact, it has been shown that condensation rates on a highly and poorly emissive surfaces were similar[19] in the steady state of condensation. Nevertheless, condensation needs to be triggered by radiative cooling. If the surface has a low emissivity, it might never reach temperatures below the dew point temperature and thus never take advantage of the contribution of water to the effective emissivity. In this context, the emissivity of the bare surface is important to initiate condensation, then emissivity will be rapidly governed by the condensed water and reach saturation for typical droplet/film size of 50 µm.

4. Experimental Section

Materials, Generation of Breath Figure Patterns and their Optical Characterization: All model surfaces were produced from 4-inch single-side polished [100]-oriented silicon wafers of low-doped (SI; resistivity of 1–20 Ω.cm). To tailor the wetting properties of the Si substrate, either i) a silica (SiO_2) layer of 470 nm was formed on a Si wafer by thermal oxidation, or ii) a layer of 30 nm of PTFE (Teflon) was deposited within a plasma reactor at 0 °C with C_4F_8 as feed gas for a duration of 10 s, leading to the ultra-thin fluorocarboned film, commonly assimilated to PTFE. The corresponding values of contact angles (CA) can be found in Figure S1a (Supporting Information) and were measured by the deposition of a droplet of DI water of 2 µL using a goniometer (Kruss, DSA 25S). To generate condensation on the different model surfaces, their temperature were set at 4 °C using a temperature-controlled stage (S-100R from Pike Technologies) and near saturated humid air (RH = 90%) at room temperature 20 °C was injected in the stage chamber in which the samples were placed. The humid air was obtained by bubbling air in a bath of ultrapure water and injected through two inlet gas nozzles at the stage chamber entrance. Airflow circulation was provided by a pump (Rena 101). Water condensation was performed on the 1 × 1 cm^2 model surfaces located on the cooling stage, itself placed on a FTIR microscope spectrometer (Spectrum 3 FTIR spectrometer coupled to Spotlight 400i imaging system). The samples were placed horizontally and the stage was cooled by a flow of fluid at −15 °C circulating through two inlet nozzles entering the stage. The stage temperature was monitored all along the experiments by using an embedded thermocouple. The chamber was sealed by a Plexiglas cover during condensation. A scheme of the setup can be found in **Figure 5** below. In these experimental conditions, the sample surface temperature is far below the dew point temperature (≈16 °C). Time was to set to zero at the beginning of condensation. Condensation was periodically interrupted by stopping the air flow to study the BFs patterns for further optical and IR characterization. *ImageJ* software was used to analyze the optical images of the breath figures taken by the FTIR microscope. The analysis consists in detecting

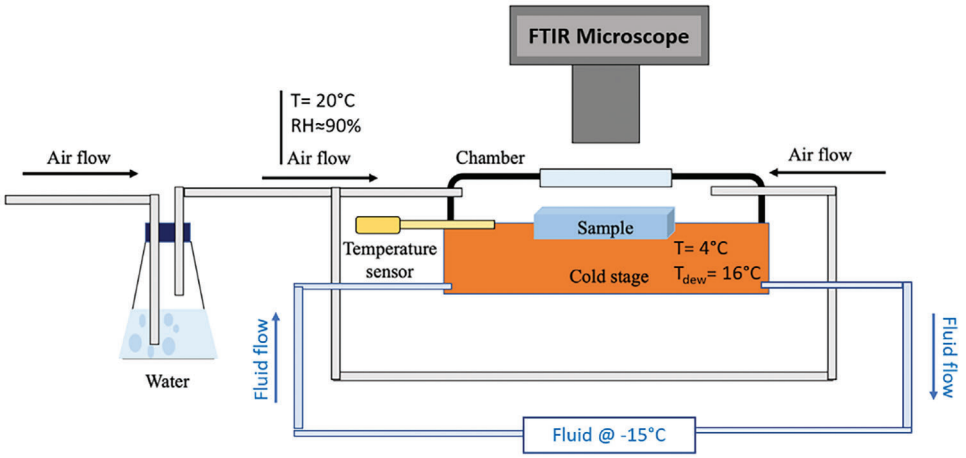

Figure 5. Scheme of the FTIR optical microscope setup under saturated humid air and controlled temperature.

drop areas on the images by an appropriate thresholding and setting the minimum detection limit at 5 μm^2. It follows the determination of the drop surface coverage and the apparent droplet radii.

Spectral Reflectance and Transmittance Measurements using FTIR Microscopy Imaging: Once the BF pattern was generated on the sample surface, the cover of stage was taken out and the reflectance and transmittance spectra images were acquired in the MWIR range using an FTIR microscopy imaging system (Perkin Elmer Spectrum 3 FTIR spectrometer coupled to a Perkin Elmer Spotlight 400i imaging system). The time of acquisition of the measurement is ≈15s, which ensures a stable BF pattern during measurement, along with a temperature of the sample maintained at 4 °C. Evaporation is strongly limited in this time scale, at such low temperature. An optical microscope image was taken just after the measurement for further characterization. The IR background was performed on a reference gold surface (for reflectance), or in air (for transmittance); prior to the measurement of IR spectra. The spectral resolution for measurements was 16 cm^{-1}, and the number of scans per pixel was 15 at a speed of 1 cm s^{-1}. The spectral range was set between 4000 cm^{-1} (2.5 µm wavelength) and 700 cm^{-1} (14.3 µm wavelength). The dimensions of the area under study were 350 × 450 μm^2. The pixel size was set to 50 µm for the assessment of the global spectral response, reflectance and transmittance were averaged by the 63 generated spectra. For the assessment of the local contribution of droplets on reflectance and transmittance in Figure 4, the pixel size was set to its minimal value of 6.25 µm, generating localized spectra on areas with dimensions 6.25 × 6.25 µm further used for the generation of the spectral images. At very large scales, relative humidity (RH) modifies the atmosphere absorptivity and then the light transmittance across the atmosphere. However, in the present experimental situation, the traveling path of the emitted light between the studied sample and the measurement device is only of a few cm and can be neglected.[38]

Note that when the spatial resolution mode was activated in the transmittance measurements it was not possible to keep the surface temperature low enough to prevent evaporation of the droplets. This evaporation is, however, slow enough such as it affects only marginally the BF pattern, as shown in Figure 4, where tiny droplets are still present.

Water Film Generation and Spectral Measurements: To generate a water film with a defined thickness and to characterize its spectral response, an experimental procedure was set as follows. Water was mixed with a small amount of Polymethyl methacrylate (PMMA) or polystyrene (PS) microspheres (Microbeads AS, Norway with a standard deviation in diameter <5%) to form a colloidal solution as described in Ref.[39] leading to a PMMA concentration in water of 2 mg mL^{-1}, which has no observable infrared light absorption compared to water. Additionally, the numerically-calculated transmittance for a system without beads (shown in Figure S6a, Supporting Information), shows a reasonably good agreement with the measurement results, with no extra peaks or trends, suggesting that the effect of the beads on transmittance is indeed negligible. The uniformity of the water thickness is granted by the numerous PMMA micro-beads acting as a spacer in-between two flat silicon pieces. Since those micro-beads have equal diameter, their uniform spread over the surface grants a uniform spacer and hence, a uniform water thickness. Then 10 µL of the solution was dispensed in between two rectangular silicon slabs (10 × 15 mm) cut from a low-doped silicon wafer of 400 µm thickness. The diameter of the spheres was chosen to be equal to the required film thickness. The spheres therefore acted as a spacer between the two silicon slabs, resulting in a precise film thickness (see Figure S6a, Supporting Information). The samples were then measured in transmission mode using Tensor II FTIR spectrometer (Bruker, Germany), with a spectral resolution of 4 cm^{-1} and an average of 16 scans.

Numerical Simulation of Reflectance and Transmittance: The transmittance and reflectance of droplets on silicon were simulated using the S4[32] implementation of the rigorous coupled-wave analysis (RCWA), where a plane wave incident at $\Theta_{in} = X^{\circ}$ was used. The simulation structure was assumed to be an array of water droplets arranged in a 2D hexagonal lattice resting on a silicon substrate. The droplet shape was assumed to be a hemisphere, where it is stair-case approximated in the normal direction into 50 layers, as required for RCWA simulation. The spacing between droplets (lattice constant) was chosen to give the adequate water fill area (S/S_{tot}). The complex refractive index of silicon[34] and water[35] as a function of wavelength were used in the simulation. The total output power in all diffraction orders (all angles) was calculated (all orders), in addition to the output power with collection limited to power emerging at angles between the specular reflection angle θ_{ref} with a certain range θ' (power emerging with angle between $\theta_{ref} - \theta'$ and $\theta_{ref} + \theta'$ are summed and power emerging with other angles is considered lost), denoted as "cone θ'". For inclined incidence, the average output power of both possible polarizations was calculated. The BFs simulations for droplets having a certain size distribution were calculated by making separate RCWA simulation for each droplet radius r_i to calculate its spectrum $S_i(\lambda) = S(\lambda; r_i)$ and weighting it with the fraction of the area filled with this droplet size obtained from the experimental results. The experimentally obtained fraction of droplets with a radius r_i is denoted by $f_{..i}$, and hence the fraction of the surface area occupied by droplets of this size is $w_i = \frac{f_i \pi r_i^2}{\Sigma_k f_k \pi r_k^2}$. The weighted average spectrum corresponding to this breath figure is then $S(\lambda) = \sum_i S_i(\lambda) w_i$.

Supporting Information

Supporting Information is available from the Wiley Online Library or from the author.

Acknowledgements

This project was funded by the METAWATER Project (No. ANR-20-CE08-0023 META-WATER) and the BROMEDIR project (No. 101092697).

Conflict of Interest

The authors declare no conflict of interest.

Author Contributions

N.L., T.B., and E.N. conceptualized the idea and designed the experiments. N.L. made investigation, data curation, figures elaboration, and wrote the original draft; N.L. conducted the experimental work. A.M.O. conducted the simulation and modeling work, the experimental work on the water films and wrote the corresponding text in Experimental Section. F.M. conducted fabrication of the samples. N.L., A.H., G.H., and A.M. contributed in building experimental setups. A.H performed the cooling power calculations. T.B. and E.N. provided financial and equipment support; A.M.O., A.M., T.B., D.B., and E.N., thoroughly reviewed the manuscript, which was then reviewed by all coauthors.

Data Availability Statement

The data that support the findings of this study are available from the corresponding author upon reasonable request.

Keywords

atmospheric water harvesting, atmospheric window, dropwise condensation, emissivity, water droplets

Received: February 24, 2024
Revised: May 10, 2024
Published online: May 21, 2024

[1] Y. Li, W. Li, T. Han, X. Zheng, J. Li, B. Li, S. Fan, C.-W. Qiu, *Nat. Rev. Mater.* **2021**, *6*, 488.
[2] L. Gao, E. Nefzaoui, F. Marty, X. Wei, S. Bastide, Y. Leprince-Wang, T. Bourouina, *Sol. Energy Mater. Sol. Cells* **2022**, *243*, 111793.
[3] G. Huang, K. Wang, C. N. Markides, *Light Sci: Appl.* **2021**, *10*, 28.
[4] K. Xu, M. Du, L. Hao, J. Mi, Q. Yu, S. Li, *J. Mater.* **2020**, *6*, 167.
[5] T. Burger, C. Sempere, B. Roy-Layinde, A. Lenert, *Joule* **2020**, *4*, 1660.
[6] E. Nefzaoui, J. Drevillon, K. Joulain, *J. Appl. Phys.* **2012**, *111*, 084316.
[7] Md. M. Hossain, M. Gu, *Adv. Sci.* **2016**, *3*, 1500360.
[8] J. Trosseille, A. Mongruel, L. Royon, D. Beysens, *Int. J. Heat Mass Transfer* **2021**, *172*, 121160.
[9] C. Blanchard, L. Wojszvzyk, C. Jamois, J.-L. Leclercq, C. Chevalier, L. Ferrier, P. Viktorovitch, I. Moldovan-Doyen, F. Marquier, J.-J. Greffet, X. Letartre, *Opt. Mater. Express* **2022**, *12*, 1.
[10] X. Liu, D. Beysens, T. Bourouina, *ACS Mater. Lett.* **2022**, *4*, 1003.
[11] D. Beysens *Dew Water*, River Publishers, Gistrup, Aalborg, Denmark **2018**.
[12] X. Liu, J. Trosseille, A. Mongruel, F. D. Marty, P. Basset, J. Laurent, L. Royon, T. Cui, D. Beysens, T. Bourouina, *iScience* **2021**, *24*, 102814.
[13] M. Lee, G. Kim, Y. Jung, K. R. Pyun, J. Lee, B.-W. Kim, S. H. Ko, *Light Sci: Appl.* **2023**, *12*, 134.
[14] J. Fei, D. Han, J. Ge, X. Wang, S. W. Koh, S. Gao, Z. Sun, M. P. Wan, B. F. Ng, L. Cai, H. Li, *Adv. Funct. Mater.* **2022**, *32*, 2203582.
[15] S. Sarkar, A. A. Elsayed, Y. M. Sabry, F. Marty, J. Drévillon, X. Liu, Z. Liang, E. Richalot, P. Basset, E. Nefzaoui, T. Bourouina, *Adv. Photonics Res.* **2023**, *4*, 2200223.
[16] V. S. Nikolayev, D. Beysens, A. Gioda, I. Milimouka, E. Katiushin, J.-P. Morel, *J. Hydrol.* **1996**, *182*, 19.
[17] O. Clus, J. Ouazzani, M. Muselli, V. S. Nikolayev, G. Sharan, D. Beysens, *Desalination* **2009**, *249*, 707.
[18] T. M. J. Nilsson, W. E. Vargas, G. A. Niklasson, C. G. Granqvist, *Renewable Energy* **1994**, *5*, 310.
[19] J. Trosseille, A. Mongruel, L. Royon, D. Beysens, *Int. J. Heat Mass Transfer* **2022**, *183*, 122078.
[20] J. F. Maestre-Valero, V. Martínez-Alvarez, A. Baille, B. Martín-Górriz, B. Gallego-Elvira, *J. Hydrol.* **2011**, *410*, 84.
[21] P. Chýlek, P. Damiano, E. P. Shettle, *J Atmos Sci.* **1992**, *49*, 1459.
[22] V. S. Nikolayev, P. Sibille, D. A. Beysens, *Opt. Commun.* **1998**, *150*, 263.
[23] Y. Huang, C. Feng, J. Hoeniges, K. Zhu, L. Pilon, *J. Quant. Spectrosc. Radiat. Transfer* **2020**, *251*, 107039.
[24] I. V. Pollet, J. G. Pieters, *J. Agri, Eng. Res.* **2000**, *75*, 65.
[25] K. P. Gurton, R. Dahmani, G. Videen, *J. Quant. Spectrosc. Radiat. Transfer* **2004**, *88*, 61.
[26] Videen, *Appl. Opt.* **2003**, *42*, 5557.
[27] M. R. Bassett, H. A. Trethowen, *J. Therm. Insul.* **1984**, *8*, 127.
[28] S. R. Delwiche, D. H. Willits, *Transactions ASAE* **1984**, *27*, 1476.
[29] R. Yang, M. Wang, M. Du, X. Wang, G. H. Tang, *Sol. Energy Mater. Sol. Cells* **2022**, *238*, 111615.
[30] E. Simsek, J. Mandal, A. P. Raman, L. Pilon, *Int. J. Heat Mass Transfer* **2022**, *198*, 123399.
[31] M. Constancio Jr, R. X. Adhikari, O. D. Aguiar, K. Arai, A. Markowitz, M. A. Okada, C. C. Wipf, *Int. J. Heat Mass Transfer* **2020**, *157*, 119863.
[32] V. Liu, S. Fan, *Computer Phys. Commun.* **2012**, *183*, 2233.
[33] S. J. Byrnes, *Multilayer Optical Calculations*, **2016**, https://doi.org/10.48550/ARXIV.1603.02720.
[34] E. Shkondin, O. Takayama, M. E. A Panah, P. Liu, P. V. Larsen, M. D. Mar, F. Jensen, A. V. Lavrinenko, *Opt. Mater. Express* **2017**, *7*, 1606.
[35] G. M. Hale, M. R. Querry, *Appl. Opt.* **1973**, *12*, 555.
[36] J. A. Sanderson, *J. Opt. Soc. Am.* **1940**, *30*, 405.
[37] J. C. Howell, T. Yizhaq, N. Drechsler, Y. Zamir, D. Beysens, J. A. Shaw, *J. Hydrol.* **2021**, *603*, 126971.
[38] W. Minkina, D. Klecha, *J. Sens. Sens. Syst.* **2016**, *5*, 17.
[39] A. M. Othman, Y. M. Sabry, D. Khalil, B. Saadany, T. Bourouina, *Anal. Methods* **2024**, *16*, 262.